Chemical Science

ROYAL SOCIETY OF CHEMISTRY

EDGE ARTICLE

View Article Online
View Journal | View Issue

Cite this: *Chem. Sci.*, 2022, **13**, 14357

All publication charges for this article have been paid for by the Royal Society of Chemistry

Structured copper-hydride nanoclusters provide insight into the surface-vacancy-defect to non-defect structural evolution†

Yizheng Bao,‡ Xiaohang Wu,‡ Bing Yin,‡ Xi Kang, Zidong Lin, Huijuan Deng, Haizhu Yu, Shan Jin,* Shuang Chen* and Manzhou Zhu*

Received 9th June 2022
Accepted 20th November 2022

DOI: 10.1039/d2sc03239b

rsc.li/chemical-science

Exploring the structural evolution of clusters with similar sizes and atom numbers induced by the removal or addition of a few atoms contributes to a deep understanding of structure–property relationships. Herein, three well-characterized copper-hydride nanoclusters that provide insight into the surface-vacancy-defect to non-defect structural evolution were reported. A surface-defective copper hydride nanocluster $[Cu_{28}(S\text{-}c\text{-}C_6H_{11})_{18}(PPh_2Py)_3H_8]^{2+}$ (**Cu_{28}-PPh_2Py** for short) with only one C_1 symmetry axis was synthesized using a one-pot method under mild conditions, and its structure was determined. Through ligand regulation, a 29th copper atom was inserted into the surface vacancy site to give two non-defective copper hydride nanoclusters, namely $[Cu_{29}(SAdm)_{15}Cl_3(P(Ph\text{-}Cl)_3)_4H_{10}]^+$ (**Cu_{29}-P(Ph-Cl)$_3$** for short) with one C_3 symmetry axis and $(Cu_{29}(S\text{-}c\text{-}C_6H_{11})_{18}(P(Ph\text{-}^pMe)_3)_4H_{10})^+$ (**Cu_{29}-P(Ph-Me)$_3$** for short) with four C_3 symmetry axes. The optimized structures show that the 10 hydrides cap four triangular and all six square-planar structures of the cuboctahedral Cu_{13} core of **Cu_{29}-P(Ph-Me)$_3$**, while the 10 hydrides cap four triangular and six square-planar structures of the anti-cuboctahedral Cu_{13} core of **Cu_{29}-P(Ph-Cl)$_3$**, with the eight hydrides in **Cu_{28}-PPh_2Py** capping four triangular and four square planar-structures of its anti-cuboctahedral Cu_{13} core. Cluster stability was found to increase sequentially from **Cu_{28}-PPh_2Py** to **Cu_{29}-P(Ph-Cl)$_3$** and then to **Cu_{29}-P(Ph-Me)$_3$**, which indicates that stability is affected by the overall structure of the cluster. Structural adjustments to the metal core, shell, and core–shell bonding model, in moving from **Cu_{28}-PPh_2Py** to **Cu_{29}-P(Ph-Cl)$_3$** and then to **Cu_{29}-P(Ph-Me)$_3$**, enable the structural evolution and mechanism responsible for their physicochemical properties to be understood and provide valuable insight into the structures of surface vacancies in copper nanoclusters and structure–property relationships.

1. Introduction

The nanoclusters continue to receive attention because of their promising catalysis, biosensing, and luminescence applications.[1–5] Owing to the quantum size effect and discrete electronic energy levels, the removal or addition of a very small number of atoms from the core or shell structure induces structural defects or structural distortions in the nanocluster that trigger significant changes in performance.[6–9] Atom-by-atom regulation can provide insight into the structural-evolution process and the mechanism responsible for how structural change affects performance.[10–12] For example, the removal of the center S atom from the $Ag_{14}S$ core in $[Ag_{62}S_{13}(SBu^t)_{32}]^{4+}$ (0e) results in the formation of a complete FCC Ag_{14} unit in $[Ag_{62}S_{12}(SBu^t)_{32}]^{2+}$ (4e) (defective structure with a hollow core), in which the presence of free valence electrons leads to photoluminescence quenching.[13–15] The traceless removal of two kernel atoms from $Au_{48}(m\text{-MBT})_{26}$ to give $Au_{46}(m\text{-MBT})_{26}$ facilitates PL emission (surface defects),[16] while a single 28th Ag atom inserted into the interstice (hole vacancy) of the outermost metal layer of the $[Ag_{27}(S^tBu)_{14}(S)_2(CF_3COO)_9(DMAc)_4]\cdot DMAc$ nanocluster gives photoluminescent $[Ag_{28}(SAdm)_{14}(S)_2(CF_3COO)_{10}(H_2O)_4]$.[17] Consequently, nanoclusters have been used as effective platforms to dissect the structural evolution of a nanomaterial from the perspective of defect chemistry and to understand how this evolution changes its properties, thereby providing rich insight into the relationship between structure and performance.[18–23]

Nowadays, well determined copper-hydride nanoclusters have also been reported, such as the $[Cu_8H_6(\mu\text{-dppm})_5](PF_6)_2$,[24] $[Cu_9H_7(\mu\text{-dpmppm})_3]X_2$, $[Cu_{16}H_{14}(\mu\text{-dpmppm})_4]X_2$,[25]

Institutes of Physical Science and Information Technology, Centre for Atomic Engineering of Advanced Materials, Key Laboratory of Structure and Functional Regulation of Hybrid Materials of Ministry of Education, Department of Chemistry, Anhui Province Key Laboratory of Chemistry for Inorganic/Organic Hybrid Functionalized Materials, Anhui University, Hefei, Anhui 230601, China. E-mail: jinshan@ahu.edu.cn; chenshuang@ahu.edu.cn; zmz@ahu.edu.cn

† Electronic supplementary information (ESI) available: Details of the synthesis process, characterization, and X-ray analysis, and Fig. S1–S30 and Tables S1–S6 offer more details on the nanoclusters. CCDC 2109287, 2109289, and 2166571. For ESI and crystallographic data in CIF or other electronic format see DOI: https://doi.org/10.1039/d2sc03239b

‡ These authors contributed equally.

$[Cu_{20}H_{11}\{E_2P(OiPr)_2\}_9$ (E = S or Se),[26,27] $[Cu_{23}(PhSe)_{16}(Ph_3P)_8(H)_6]\cdot BF_4$,[28] $[Cu_{25}H_{22}(PR_3)_{12}]Cl$,[29,30] $[Cu_{28}H_{15}\{S_2CN(nPr)_2\}_{12}](PF_6)$,[31] $[Cu_{28}H_{20}(S_2P(O^iPr)_2)_9]^-$,[32] $[Cu_{28}H_{16}(dppp)_4(RS)_4(CF_3CO_2)_8]$,[33] $[Cu_{30}H_{18}\{E_2P(OR)_2\}_{12}]$(E = S or Se; R = ^{n}Pr,^{i}Pr or ^{i}Bu),[34] $Cu_{32}H_{20}\{S_2PR_2\}_{12}]$,[35,36] $[Cu_{53}(RCOO)_{10}(C{\equiv}C^tBu)_{20}Cl_2H_{18}]^+$,[37] $[Cu_{61}(S^tBu)_{26}S_6Cl_6H_{14}]^+$ (ref. 38) and $[Cu_{81}(PhS)_{46}(tBuNH_2)_{10}(H)_{32}]^{3+}$.[39] And the copper-hydride nanoclusters have drawn increasing research interest because they have aesthetically fascinating molecular structures and are potentially useful in catalysis, hydrogen storage, and photovoltaics applications.[8,37,40–43] In contrast to the numerous reports on the structural evolution of gold/silver clusters, examining the structural evolution of copper-hydride clusters remains challenging owing to difficulties associated with synthesizing and crystallizing copper-hydride nanoclusters. A reversible transformation between $[Cu_7(H)\{S_2CR\}_6]$ and $[Cu_8(H)\{S_2CR\}_6](PF_6)$, a defect to defect-growth-based copper hydride cluster was reported by the Liu group.[44] Metal exchanging Pt^{4+} ions into $[Cu_{32}(PET)_{24}Cl_2H_8]^{2-}$ resulted in $[Pt_2Cu_{34}(PET)_{22}Cl_4]^{2-}$, an internal-defective nanocluster.[45,46] The surface vacancy defective $[Cu_{36}H_{10}(PET)_{24}(PPh_3)_6Cl_2]$ nanoclusters and the hypothetical non-defective half-cubic copper hydride $[Cu_{38}H_{10}(SC_6H_3F_2)_{26}(PPh_3)_8]^{2+}$ nanocluster were considered to be other examples of copper-hydride structural evolution that revealed surface metal atom vacancies, ligand defects, and skeletal distortion.[47] Although studies on defect clusters have been reported, there are few studies on the effects of surface defects and regrowth on structure and properties because only a few series of copper-hydride clusters are well determined, let alone studies on structural evolution driven in an atom-by-atom manner in a copper-hydride.[7,8,44,48,49]

Herein, we report three novel well-determined Cu-hydride nanoclusters that provide insight into surface-vacancy-defect to non-defect structural evolution: surface-defective $[Cu_{28}(S\text{-}c\text{-}C_6H_{11})_{18}(PPh_2Py)_3H_8]^{2+}$ (**Cu_{28}-PPh_2Py**), and non-defective $[Cu_{29}(SAdm)_{15}Cl_3(P(Ph\text{-}Cl)_3)_4H_{10}](PF_6)$ (**Cu_{29}-P(Ph-Cl)$_3$**) and $Cu_{29}(S\text{-}c\text{-}C_6H_{11})_{18}(P(Ph\text{-}^pMe)_3)_4H_{10}(BF_4)$ (**Cu_{29}-P(Ph-Me)$_3$**). Structural analyses of the surface vacancy-defective **Cu_{28}-PPh_2Py** and non-defective **Cu_{29}-P(Ph-Cl)$_3$/Cu_{29}-P(Ph-Me)$_3$** provide deep insight into how surface vacancy defects structurally evolve into non-defects, including differences in the metal core, number of hydrogen ligands, packing model, metal shell, and core–shell bonding model. Interestingly, **Cu_{29}-Ph-^{p}Me** has a virtually identical structure to that of the $MAg_{28}(SR)_{18}(PR'_3)_4$ silver nanocluster in terms of the number of metal atoms, the thiol and phosphine ligand counts, and the atomic arrangement, despite the presence of hydrogen.[50] The structural evolution provides an understanding of how surface vacancy defects structurally evolve and provides valuable insight into the structures of surface vacancies in copper nanoclusters as well as structure–property relationships.

2. Methods

2.1 Chemicals

Tetrakis(acetonitrile)copper(I) tetrafluoroborate ($[Cu(CH_3CN)_4]\cdot BF_4$, 98%), tetrakis(acetonitrile)copper(I) hexafluorophosphate ($[Cu(CH_3CN)_4]\cdot PF_6$, 98%), diphenyl-2-pyridylphosphine (PPh_2Py, 97%), tri(*p*-tolyl)phosphine (P(Ph-^{p}Me)$_3$, 98%), tris(4-chlorophenyl)phosphine(P(Ph-^{p}Cl)$_3$, 98%), cyclohexyl mercaptan ($C_6H_{12}S$, ≥99%), 1-adamantanethiol (1-AdmSH, 98%), sodium borohydride ($NaBH_4$, 98%), sodium borodeuteride ($NaBD_4$, 98%), acetonitrile (CH_3CN), chloroform ($CHCl_3$), chloroform-d ($CDCl_3$), methanol (MeOH), ethanol (EtOH), dichloromethane (CH_2Cl_2), and *n*-hexane (Hex) were obtained from commercial sources and used as received.

2.2 Synthesis of $[Cu_{28}(C_6H_{11}S)_{18}(PPh_2Py)_3(H)_8][BF_4]_2$ nanoclusters (Cu_{28}-PPh_2Py-H)

$[Cu_{28}(C_6H_{11}S)_{18}(PPh_2Py)_3(H)_8][BF_4]_2$ was prepared by dissolving $[Cu(CH_3CN)_4]\cdot BF_4$ (160 mg, 0.51 mmol) in 1 : 1 (v/v) CH_3CN/$CHCl_3$ (10 mL). After 10 min, PPh_2Py (100 mg, 0.40 mmol) was added to the solution, followed by $C_6H_{11}SH$ (22 μL, 0.18 mmol), and the mixture was vigorously stirred. After 20 min, a freshly prepared solution of $NaBH_4$ (30 mg, 0.8 mmol, dissolved in 2 mL MeOH) was added dropwise to the aforementioned solution, which immediately turned brown. The mixture was stirred for 5 h at room temperature, at which time a bright orange precipitate of the product had formed at the bottom of the flask. The product was collected and recrystallized from CH_2Cl_2/Hex over several days at room temperature.

2.3 Synthesis of $[Cu_{28}(C_6H_{11}S)_{18}(PPh_2Py)_3(D)_8][BF_4]_2$ nanoclusters (Cu_{28}-PPh_2Py-D)

Cu_{28}-PPh_2Py-D was synthesized similarly to **Cu_{28}-PPh_2Py-H**, with the exception that $NaBD_4$ (40 mg, 1 mmol) was used as the reducing agent.

2.4 Synthesis of $[Cu_{29}(SAdm)_{15}Cl_3(P(Ph\text{-}Cl)_3)_4H_{10}](PF_6)$ nanoclusters (Cu_{29}-P(Ph-Cl)$_3$-H)

Cu_{29}-P(Ph-Cl)$_3$-H was prepared by dissolving $[Cu(CH_3CN)_4]\cdot PF_6$ (100 mg, 0.27 mmol) in 1 : 1 (v/v) CH_3CN/$CHCl_3$ (10 mL) After 10 min, P(Ph-^{p}Cl)$_3$ (100 mg, 0.27 mmol) was added to the solution, followed by 1-AdmSH (50 mg, 0.30 mmol) and the mixture was stirred vigorously. After 20 min, a freshly prepared solution of $NaBH_4$ (60 mg, 1.6 mmol, dissolved in 2 mL MeOH) was added. The mixture was stirred at room temperature for 10 h. The product was collected and recrystallized from CH_2Cl_2/Hex over several days at room temperature. Although no chloride was used in the synthesis, the capping Cl atoms in **Cu_{29}-P(Ph-Cl)$_3$** can be reasonably considered to be derived from the solvent $CHCl_3$, similar to previous reports of some Cl ligand-containing clusters.[51,52]

2.5 Synthesis of $[Cu_{29}(SAdm)_{15}Cl_3(P(Ph\text{-}Cl)_3)_4D_{10}](PF_6)$ nanoclusters (Cu_{29}-P(Ph-Cl)$_3$-D)

The synthesis of **Cu_{29}-P(Ph-Cl)$_3$-D** is similar to that of **Cu_{29}-P(Ph-Cl)$_3$-H**, except that the reducing agent is changed to 64 mg $NaBD_4$ (1.6 mmol).

2.6 Synthesis of $[Cu_{29}(SC_6H_{11})_{18}((Ph\text{-}^pMe)_3P)_4H_{10}][BF_4]$ nanoclusters (Cu_{29}-P(Ph-Me)$_3$-H)

Cu_{29}-P(Ph-Me)$_3$-H was prepared following the procedure used to synthesize **Cu_{28}-PPh_2Py-H**, with the exception that tri(*p*-tolyl) phosphine ((Ph-^{p}Me)$_3$P) (116 mg, 0.38 mmol) was used instead

of PPh_2Py (100 mg, 0.40 mmol). Red crystals were obtained by recrystallization from CH_2Cl_2/Hex over one week.

2.7 Synthesis of $[Cu_{29}(C_6H_{11}S)_{18}((Ph\text{-}^{P}Me)_3P)_4D_{10}][BF_4]$ nanoclusters (Cu_{29}-Ph-^{P}Me-D)

Cu_{29}-P(Ph-^{P}Me)$_3$-D was synthesized similarly to **Cu_{29}-P(Ph-Me)$_3$-H**, with the exception that $NaBD_4$ (40 mg, 1 mmol) was used instead of $NaBH_4$ (30 mg, 0.8 mmol).

2.8 Characterization

All UV-vis spectra of the nanoclusters were recorded on a Metash UV-6000PC UV-vis spectrophotometer, and the samples were dissolved in CH_2Cl_2 whose background correction was made using a CH_2Cl_2 blank. X-ray photoelectron spectroscopy (XPS) measurements were performed using a Thermo ESCALAB 250 configured with a monochromated Al Kα (1486.8 eV) 150 W X-ray source, a 0.5 mm circular spot size, a flood gun to counter charging effects, and an analysis chamber base pressure lower than 1×10^{-9} mbar, and the data were collected with an FAT of 20 eV. Electrospray ionization (ESI) mass spectrum was obtained on a Waters XEVO G2-XS QT of mass spectrometer. The samples are dissolved in a mixture solution of CH_2Cl_2/CH_3OH (v/v = 1 : 1), which is directly infused into the chamber at 10 μL min^{-1} with positive mode. Nuclear magnetic resonance (NMR) analysis was performed on a Bruker Avance spectrometer operating at 400 MHz. CD_2Cl_2 was used as the solvent to dissolve the crystals of copper-hydride clusters; the residual solvent peak (*i.e.*, 1H at 5.32 ppm) was used as the reference. The clusters were dissolved in CH_2Cl_2 for the ^{2}H NMR spectra. Data collection for single-crystal X-ray diffraction was carried out using a Stoe Stadivari diffractometer under a liquid nitrogen flow at 150 K, using graphite-monochromatized Cu Kα radiation (λ = 1.54186 Å). Data reductions and absorption corrections were performed using SAINT and SADABS programs.

3. Results and discussion

The **Cu_{28}-PPh$_2$Py**, **Cu_{29}-P(Ph-Cl)$_3$**, and **Cu_{29}-P(Ph-Me)$_3$** series of copper nanoclusters were directly synthesized using a one-pot method under mild conditions. Briefly, **Cu_{28}-PPh$_2$Py** was synthesized by dissolving $[Cu(CH_3CN)_4]BF_4$ in a mixture of acetonitrile (CH_3CN) and chloroform ($CHCl_3$) at room temperature, after which $C_6H_{11}SH$ and PPh_2Py were added, and $NaBH_4$ was used as the reducing agent. The solution turned dark red. The orange crystals were characterized by single-crystal X-ray crystallography (SC-XRC) (Fig. S1†). **Cu_{28}-PPh$_2$Py** crystallized in the monoclinic *P*21/*a* space group (Table S1†). On the other hand, **Cu_{28}-PPh$_3$** (Fig. S2†) crystallized in the monoclinic *I*2/*a* space group (Table S2†). **Cu_{29}-Ph-^{P}Me** was obtained when the P(Ph-^{P}Me)$_3$ ligand was used instead of PPh_2Py under the same conditions (Fig. S3†). Red **Cu_{29}-Ph-^{P}Me** crystallized in the trigonal $R\bar{3}$ space group (Table S3†).

The structures of **Cu_{28}-PPh$_2$Py**, **Cu_{29}-P(Ph-Cl)$_3$**, and **Cu_{29}-P(Ph-Me)$_3$** are shown in Fig. 1. **Cu_{28}-PPh$_2$Py/PPh$_3$** contains 28 Cu atoms, 18 S-*c*-C_6H_{11} ligands, eight hydrides, and three PPh_2Py ligands (Fig. 1A and B). A surface vacancy defect located in the

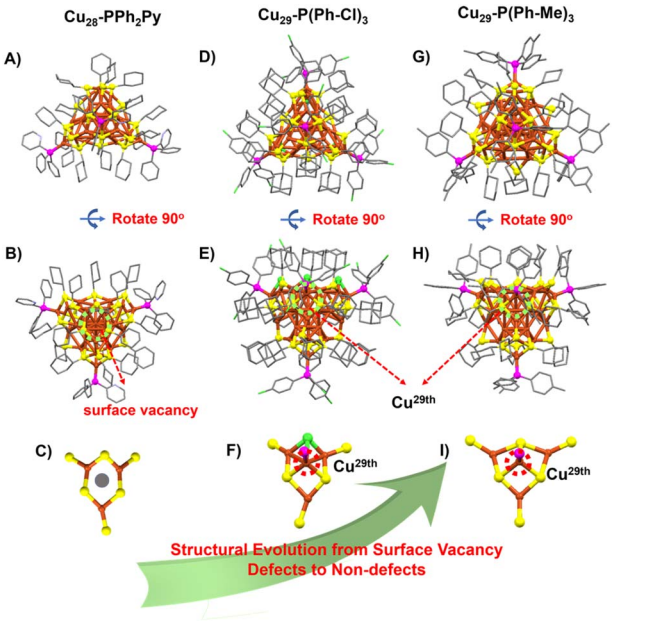

Fig. 1 The overall structures of the series of copper nanoclusters. (A–C) **Cu_{28}-PPh$_2$Py**, (D–F) **Cu_{29}-P(Ph-Cl)$_3$**, and (G–I) **Cu_{29}-P(Ph-Me)$_3$** and the Cu^{29th} sites. Color scheme: copper = Cu, yellow = S, purple = P, blue-purple = N, green = Cl, and gray = C. H atoms are omitted for clarity.

$Cu_3(SR)_6$ motif is observed in **Cu_{28}-PPh$_2$Py** (Fig. 1C). The copper skeletons of **Cu_{29}-P(Ph-Cl)$_3$** and **Cu_{29}-P(Ph-Me)$_3$** formed (Fig. 1D–I) when the 29th copper atom was inserted into the interstice (surface vacancy site) (Fig. 1F and I). The formed **Cu_{29}-P(Ph-Cl)$_3$** possesses 29 Cu atoms, 15-SAdm ligands, 3 Cl atoms, 10 hydrides, and four (P(Ph-Cl)$_3$). Similarly, **Cu29-P(Ph-Me)$_3$** possesses 29 Cu atoms, 18 S-*c*-C_6H_{11} ligands, 10 hydrides, and four P(Ph-^{P}Me)$_3$ ligands, with four P(Ph-^{P}Me)$_3$ units occupying the four vertices of the tetrahedron. As shown in Fig. S4–S6,† the **Cu_{28}-PPh$_2$Py** framework possesses a C_1 symmetry axis, whether observed from the position of the three phosphine ligands or the vacancy (Fig. S4†). On the other hand, the **Cu_{29}-P(Ph-Cl)$_3$** framework possesses one C_3 symmetry axis, indicative of improved symmetry (Fig. S5†), while the **Cu_{29}-P(Ph-Me)$_3$** framework forms a standard tetrahedral configuration with four C_3 symmetry axes (Fig. S6†). Once again, the **Cu_{29}-Ph-^{P}Me** cluster exhibits significantly improved symmetry, affecting the copper-hydride nanocluster's stability. The novel changes observed for the metal core, the number of hydrogen ligands, the packing model, the metal shell, and the core/shell bonding model facilitate a detailed understanding of the surface-vacancy-defect to non-defect structural evolution.

The changes observed during structural evolution can be understood in detail by splitting the structure. The structural anatomy of surface-defective **Cu_{28}-PPh$_2$Py** is shown in Fig. 2A, which reveals that the Cu_{13} copper kernel has an anti-cuboctahedral structure. The Cu–Cu distances in the anti-cuboctahedron vary between 2.459 and 2.787 Å, with an average value of 2.605 Å. The anti-cuboctahedron Cu_{13} is surrounded by a $Cu_{15}(SR)_{18}P_3$ cage shell, which can be viewed as an

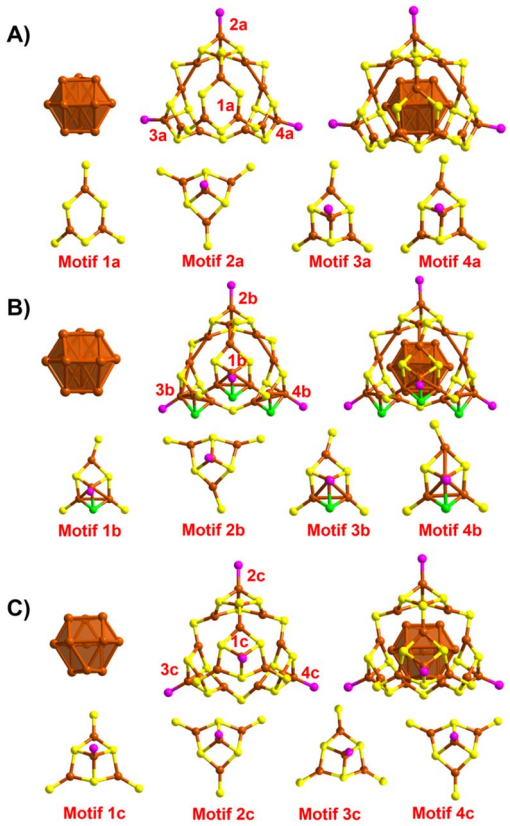

Fig. 2 Structural anatomies of the series of copper nanoclusters. (A) Cu_{28}-PPh_2Py, (B) Cu_{29}-$P(Ph\text{-}Cl)_3$, and (C) Cu_{29}-$P(Ph\text{-}Me)_3$. Color scheme: copper = Cu, yellow = S, purple = P, and green = Cl.

assembly of a single $Cu_3(SR_6)$ (Motif 1a) and three $Cu_4S_6P_1$ motifs (Motifs 2a–4a). While Motifs 2a–4a share the same molecular formula, their geometries differ. In contrast, Motif 1a has surface vacancy defects. Non-defective **Cu_{29}-$P(Ph\text{-}Cl)_3$** capped by $P(Ph\text{-}Cl)_3$, SAdm-, and Cl^- and H^- ligands was obtained (Fig. 2B) when the 29th copper atom was inserted into the surface vacancy site of Motif 1a. An anti-cuboctahedral Cu_{13} core, similar to the anti-cuboctahedral Ag_{13} core in Ag_{19} and Ag_{25} (ref. 53) was observed for **Cu_{29}-$P(Ph\text{-}Cl)_3$** by comparison with the structure of **Cu_{28}-PPh_2Py**. The anti-cuboctahedral Cu_{13} core is further capped by a $Cu_{16}(SR)_{15}P_4$ shell assembled by using $Cu_4(SR)_6P_1$ (Motif 2b) and three $Cu_4(SR)_5ClP_1$ units (Motifs 2a, 2c, and 2d). Because the AdmSH ligand is very sterically hindering, another thiol ligand cannot be accommodated; hence, the small Cl acts as a protective ligand to maintain the stability of the **Cu_{29}-$P(Ph\text{-}Cl)_3$** structure. Another non-defective **Cu_{29}-$P(Ph\text{-}Me)_3$** nanocluster capped by $P(Ph\text{-}Me)_3$, S-*c*-C_6H_{11}- and H^- ligands is shown in Fig. 2C. In contrast to the anti-cuboctahedral Cu_{13} core of **Cu_{28}-PPh_2Py** and **Cu_{29}-$P(Ph\text{-}Cl)_3$**, the Cu_{13} core in **Cu_{29}-$P(Ph\text{-}Me)_3$** is cuboctahedral in structure. The cuboctahedral Cu_{13} framework was also observed in $[Cu_{13}(S_2CNnBu_2)_6(C{\equiv}CR)_4](PF_6)$.[54,55] The Cu–Cu distances in the cuboctahedron vary between 2.457 and 2.878 Å, with an average value of 2.651 Å. The cuboctahedral Cu_{13} core is surrounded by a $Cu_{16}(SR)_{18}P_4$ shell assembled using four identical $Cu_4S_6P_1$ motifs (Motifs 1c–4c). The structure of **Cu_{29}-$P(Ph\text{-}Me)_3$** is consistent with that of a standard tetrahedron, in which the **Cu_{29}-$P(Ph\text{-}Me)_3$** frame has the same structure as $MAg_{28}(SR)_{18}(PR'_3)_4$ (Fig. S7†).

Furthermore, surface-kernel structural transfer provides diverse bonding patterns during structural evolution. First, both the cuboctahedral and anti-cuboctahedral Cu_{13} cores have eight triangular (Cu_3) surfaces and quadrilateral (Cu_4) surfaces (Fig. S8†). As shown in Fig. 3A, **Cu_{28}-PPh_2Py** has one $Cu_4(SR)_6P_1$ motif (marked with a red circle) that covers one triangular Cu_3 surface, two $Cu_4(SR)_6P_1$ motifs (marked with green circles) that cover quadrilateral (Cu_4) surfaces, as well as one $Cu_3(SR)_6$ motif (marked with a yellow circle) containing the surface vacancy defect that also covers a quadrilateral (Cu_4) surface. A vertex Cu–P resulting from the spatial position of the thiol ligand located within the $Cu_3(SR)$ ring is the difference between the $Cu_4(SR)_6P_1$ units (marked with green circles) and the $Cu_3(SR)_6$ moiety (marked with a yellow circle). As shown in Fig. S9,† when the carbon tails of the three thiol ligands in the $Cu_3(SR)_6$ ring are aligned outwards, the reserved space can support a vertex Cu–P staple insertion to form $Cu_4(SR)_6P_1$, while there is insufficient reserved space to support a vertex Cu–P staple when one thiol-ligand carbon tail is arranged inward, resulting in surface vacancy defects. This observation reveals that the orientation of

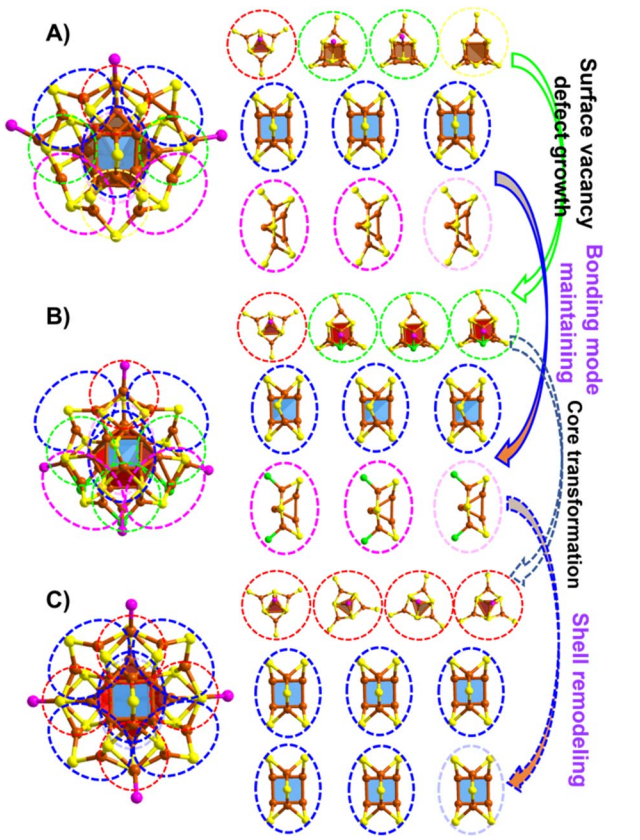

Fig. 3 The detailed core/shell bonding modes. The bonding modes in (A) Cu_{28}-PPh_2Py, (B) Cu_{29}-$P(Ph\text{-}Cl)_3$, and (C) Cu_{29}-$P(Ph\text{-}Me)_3$. Structures marked with circles of the same color are of the same type. Color scheme: copper = Cu, yellow = S, purple = P, and green = Cl.

the ligand carbon tail affects the formation of surface-vacancy defects. In addition, its bonding mode includes three quadrilateral Cu_4 units capped by $Cu_2(SR)_5$ shells (marked with blue circles) and three triangular Cu_3 units capped by $Cu_2(SR)_5$ shells (marked with purple circles). For non-defective **Cu_{29}-P(Ph-Cl)$_3$**, the $Cu_4(SR)_6P_1$ motif marked with a red circle also covers a triangular Cu_3 surface, and the three $Cu_4(SR)_5ClP_1$ motifs marked with green circles also cover quadrilateral Cu_4 surfaces (Fig. 3B). Three quadrilateral Cu_4 moieties capped by $Cu_2(SR)_5$ shells (marked with blue circles) and three triangular Cu_3 units capped by $Cu_2(SR)_4Cl$ shells (marked with purple circles) are also present, as observed in the structure of **Cu_{28}-PPh$_2$Py**. For **Cu_{29}-P(Ph-Cl)$_3$**, the capping Cl and AdmSH ligands endow enough space to support the insertion of Cu–P to form non-defective clusters (Motif 1a *vs.* Motif 1b in Fig. 2). Structural evolution from the surface-vacancy-defective **Cu_{28}-PPh$_2$Py** to non-defective **Cu_{29}-P(Ph-Cl)$_3$** involves the growth of defect motifs, with the bonding mode between the core and the motif maintained to a certain degree. The other non-defective **Cu_{29}-P(Ph-Me)$_3$** structure contains four $Cu_4(SR)_6P_1$ motifs that cover four triangular surfaces (Cu_3) of cuboctahedral Cu_{13} (marked with red circles). The spatial arrangement of thiol ligands can better support the insertion of Cu–P, forming four identical $Cu_4S_6P_1$ motifs. All six $Cu_2(SR)_5$ shells cover the quadrilateral Cu_4 unit (marked with blue circles) (Fig. 3C).

Structural evolution involves the growth of surface vacancy defects from surface-vacancy-defective **Cu_{28}-PPh$_2$Py** to non-defective **Cu_{29}-P(Ph-Cl)$_3$**, accompanied by core and bond pattern maintenance (Fig. 3A *vs.* Fig. 3B). Structural evolution involves the transformation of the **Cu_{29}-P(Ph-Cl)$_3$** core and remodeling of the **Cu_{29}-P(Ph-Cl)$_3$** shell, respectively, to form the other non-defective **Cu_{29}-P(Ph-Me)$_3$** (Fig. 3B *vs.* Fig. 3C). These results provide atomically precise insights into the defect-induced readjustment of the local structure.

Single-crystal X-ray crystallography (SCXRC) revealed both the intramolecular structure and intermolecular packing mode of the metal nanoclusters during structural evolution. **Cu_{28}-PPh$_2$Py** and **Cu_{29}-P(Ph-Cl)$_3$** only exhibit 2H arrangements with "AB" packing sequences (Fig. S10 and S11†), while the crystalline unit cell of **Cu_{29}-P(Ph-Me)$_3$** shows a special "ABCDEF" stacking sequence. The **Cu_{29}-Ph-^{P}Me** nanoclusters in the stacking layer are uniformly arranged and each nanocluster is surrounded by six identical nanoclusters with the same tropism, as shown in Fig. S12.† Such a 6H pattern was previously only observed in Au_{60} reported by Wu *et al.*[56]

The UV-vis spectra of **Cu_{28}-PPh$_2$Py**, **Cu_{29}-P(Ph-Cl)$_3$**, and **Cu_{29}-P(Ph-Me)$_3$** in CH_2Cl_2 are shown in Fig. S13.† Several weak absorptions are observed at 256 and 400 nm for **Cu_{28}-PPh$_2$Py**, at 270, 326, and 415 nm for **Cu_{29}-P(Ph-Cl)$_3$**, and at 410, 325, and 266 nm for **Cu_{29}-P(Ph-Me)$_3$**. Because determining the number of hydrogen atoms by SC-XRD is difficult, careful ESI-MS was used to determine the valence and molecular formula of each cluster and the number of hydrides. Positive-mode ESI-MS data for **Cu_{28}-PPh$_2$Py**, **Cu_{29}-P(Ph-Cl)$_3$**, and **Cu_{29}-P(Ph-Me)$_3$** are shown in Fig. 4. The spectrum of **Cu_{29}-Ph-^{P}Me** shows a prominent peak corresponding to a +1 charge at m/z = 5144.69 Da, which is attributable to $[Cu_{29}(S\text{-}c\text{-}C_6H_{11})_{18}(P(Ph\text{-}^{P}Me)_3)_4H_{10}]^+$ (Fig. 4A). The experimentally observed isotope pattern for $[Cu_{29}(S\text{-}c\text{-}C_6H_{11})_{18}(P(Ph\text{-}^{P}Me)_3)_4H_{10}]^+$ is in good agreement with the calculated pattern (Fig. S14A†). **Cu_{29}-P(Ph-Me)$_3$-D** was synthesized and subjected to ESI-MS to further confirm the presence and number of hydrides. A prominent peak corresponding to a +1 charge was observed at m/z = 5154.66 Da, which is attributable to $[Cu_{29}(S\text{-}c\text{-}C_6H_{11})_{18}(P(Ph\text{-}^{P}Me)_3)_4D_{10}]^+$ (Fig. 4B). Accordingly, 10 hydrides are present in the **Cu_{29}-P(Ph-Me)$_3$** cluster. Similarly, the ESI-MS spectrum of **Cu_{29}-P(Ph-Cl)$_3$** confirmed that it is complex (Fig. 4C and D). First, the prominent peak corresponding to a charge of +1 observed at m/z = 4468.27 Da belongs to $[Cu_{29}(SC_{10}H_{15})_{15}Cl_3H_{10}]^+$ derived from the removal of four $P(Ph\text{-}Cl)_3$ ligands from the complete $[Cu_{29}(SC_{10}H_{15})_{15}Cl_3(P(Ph\text{-}Cl)_3)_4H_{10}]^+$, and it is fully consistent with the calculated result (Fig. S14B†). Neighboring peaks at 4433.32 and 4396.33 Da are attributable to $[Cu_{29}(SC_{10}H_{15})_{15}Cl_3H_{10}\text{-}Cl]$ and $[Cu_{29}(SC_{10}H_{15})_{15}Cl_3H_{10}\text{-}2Cl]$, respectively. The difference of 10 Da between the m/z values of **Cu_{29}-P(Ph-Cl)$_3$-H** and **Cu_{29}-P(Ph-Cl)$_3$-D** indicates the presence of 10 hydrogen atoms. By comparison, the ESI-MS spectrum of $[Cu_{28}(S\text{-}c\text{-}C_6H_{11})_{18}(Ph_2PyP)_3H_8]^{2+}$ was more complicated, with peaks corresponding to charges of +1, +2, and +3 observed. Specifically, the +1 signal

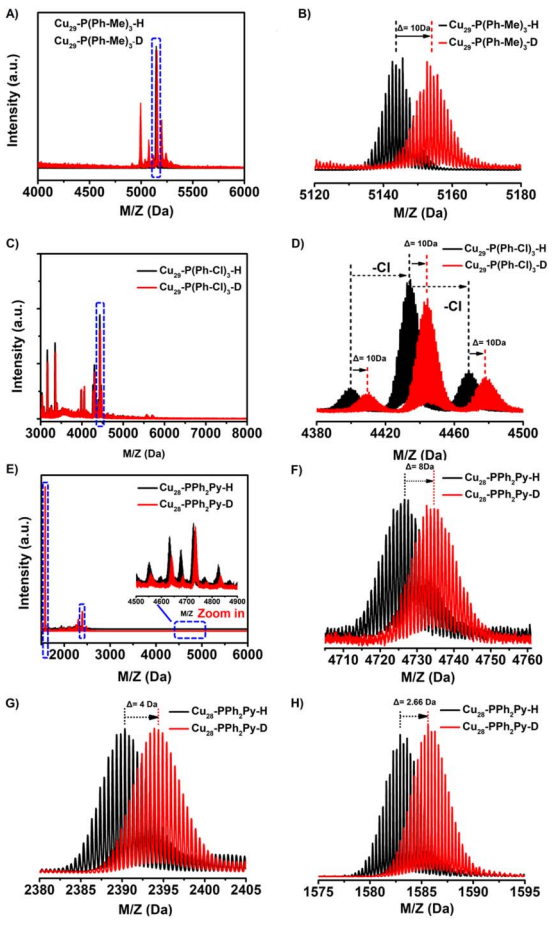

Fig. 4 ESI-MS of the series of copper nanoclusters. Positive-mode ESI-MS spectra of (A and B) **Cu_{29}-P(Ph-Me)$_3$**, (C and D) **Cu_{29}-P(Ph-Cl)$_3$**, and (E–H) **Cu_{28}-PPh$_2$Py**.

at m/z = 4726.34 Da is attributable to $[Cu_{28}(C_6H_{11}S)_{18}(C_{17}H_{14}NP)_3(H)_8 + Cl + CH_3CN]^+$, while that corresponding to a charge of +2 at m/z = 2390.55 Da is attributable to $[Cu_{28}(C_6H_{11}S)_{17}(C_{17}H_{14}NP)_3(H)_8 + Cl + (CH_3CN)(CH_2Cl_2)_2]^{2+}$, consistent with the one thiol moiety in $[Cu_{28}(C_6H_{11}S)_{18}(C_{17}H_{14}NP)_3(H)_8]^{2+}$ replaced by Cl. The +3 peak at m/z = 1583.35 Da is attributable to $[Cu_{28}(S\text{-}c\text{-}C_6H_{11})_{18}(C_{17}H_{14}NP)_3H_8 + CuCl]^{3+}$ (Fig. 4E–H and isotopic patterns in Fig. S14C–E†). We also synthesized and characterized **Cu_{28}-PPh_2Py-D**. The intervals between the 3+, 2+, and 1+ peaks of **Cu_{28}-PPh_2Py-H** and **Cu_{28}-PPh_2Py-D** were found to be 2.66, 4, and 8, respectively, consistent with the presence of eight hydrogen atoms (*i.e.*, 2.66 × 3/4 × 2/8 × 1). Although no BF_4^- counterion was found in the unit cell of **Cu_{28}-PPh_2Py**, its presence was confirmed by ESI-MS (Fig. S25†). So, combining these experimental results, none of the three copper hydride clusters have free electrons (28(Cu $4s^1$) − 18 (SR) − 8 (H-) − 2 (charge) = 0e for **Cu_{28}-PPh_2Py**, 29 (Cu $4s^1$) − 15 (SR) − 3 (Cl) − 10 (H–) − 1 (charge) = 0e for **Cu_{29}-P(Ph-Cl)$_3$** and 29 (Cu $4s^1$) − 18 (SR) − 10 (H–) − 1 (charge) = 0e for **Cu_{29}-P(Ph-Me)$_3$**).

X-ray photoelectron spectroscopy (XPS) was used to analyze the chemical compositions and copper-charge states in **Cu_{28}-PPh_2Py**, **Cu_{29}-P(Ph-Cl)$_3$**, and **Cu_{29}-P(Ph-Me)$_3$** (Fig. S20–S24†), with the Cu_{2p}, S_{2p}, P_{2p}, F_{1s}, and N_{1s} XPS spectra shown in Fig. S20–S23.† The F_{1s} signals are ascribable to the BF_4^-/PF_6^- counter ions. The presence of "BF_4^-" in the **Cu_{28}-PPh_2Py** nanocluster was also confirmed by ESI-MS (Fig. S25†). Simple XPS cannot accurately determine the specific valence states of copper in copper nanoclusters because the Cu $2p_{3/2}$ binding energies of Cu_0 and the Cu^+ in Cu_2S are identical (932.6 eV);[57] Therefore, Cu Auger-electron spectroscopy is required to further determine the specific valence states of copper. The Auger spectra of **Cu_{28}-PPh_2Py**, **Cu_{29}-P(Ph-Cl)$_3$**, and **Cu_{29}-P(Ph-Me)$_3$** show only one main Cu LMM peak at 570.69 eV (Fig. S24†), which corresponds to the Cu +1 oxidation state. Moreover, the three clusters exhibited no observable signal near 943 eV, consistent with the absence of Cu(II) in **Cu_{28}-PPh_2Py**, **Cu_{29}-P(Ph-Cl)$_3$**, and **Cu_{29}-P(Ph-Me)$_3$**.

The structural evolution from **Cu_{28}-PPh_2Py** to **Cu_{29}-P(Ph-Cl)$_3$** and then to **Cu_{29}-P(Ph-Me)$_3$** may lead to changes in the positions of the hydrogen atoms. Trying to grow single crystals of suitable quality for neutron diffraction is challenging.[26b,27,31,35] So, DFT calculations and HNMR spectra were often used for validating possible plausible locations for hydrogen.[26a,38,39,45,47] To determine the hydride locations in **Cu_{28}-PPh_2Py**, **Cu_{29}-P(Ph-Cl)$_3$**, and **Cu_{29}-P(Ph-Me)$_3$**, density functional theory (DFT) calculations to optimize their positions based on the X-ray crystallographic structures were performed first.[26a,38,39,45,47,58] In previous reports, it was found that for copper clusters, the positions of hydrogens in structures with similar moieties have a certain similarity, for example, the positions of 6 hydrogens in $Cu_{32}H_{20}$ are found to be similar to their structural positions in $Cu_{20}H_{11}$.[8,26b,35] Inspired by these research reports, and given the number of hydrides and the similarity in Cu@Cu_{12} kernel structures as well as the motifs of **Cu_{28}-PPh_2Py**, **Cu_{29}-P(Ph-Cl)$_3$**, **Cu_{29}-P(Ph-Me)$_3$** and $[Cu_{25}(SPhCl_2)_{18}H_{10}]^{3-}$ (anti-cuboctahedral Cu_{25}), the locations of the hydrides in **Cu_{28}-PPh_2Py**, **Cu_{29}-P(Ph-Cl)$_3$**, and **Cu_{29}-P(Ph-Me)$_3$** were determined referring to that of $[Cu_{25}(SPhCl_2)_{18}H_{10}]^{3-}$, while the positions of hydrogens in Cu_{25} (Fig. 5A), which served as references, were carefully determined by the Zheng group *via* HNMR spectroscopy and DFT calculations.[59] These optimized structures can remain stable, indicating that the determined hydrogen positions are reasonable. Fig. 5 shows that all hydrides are located around the M_{13} core. Half of the eight triangular structures and all six square-planar structures of the Cu_{13} core surface in **Cu_{29}-P(Ph-Me)$_3$** are capped with one hydride each (Fig. 5B). Meanwhile, **Cu_{28}-PPh_2Py** shares the same icosahedral structure as Cu_{25}, and its eight hydrides are separated into two groups: four capping the triangular structure and another four capping the square-planar structure of the Cu_{13} core surface (Fig. 5C). Another **Cu_{29}-P(Ph-Cl)$_3$** cluster was obtained, whose Cu@Cu_{12} core is the same as that of the Cu_{25} core and **Cu_{28}-PPh_2Py**, which are both cuboctahedral. The ten H atoms of **Cu_{29}-P(Ph-Cl)$_3$** cover all square faces and half of the triangular faces (Fig. 5D). The maintained frameworks of the proposed structures of the aforementioned **Cu_{29}-P(Ph-Me)$_3$**, **Cu_{29}-P(Ph-Cl)$_3$**, and **Cu_{28}-PPh_2Py** clusters (denoted as **Cu_{29}-P(Ph-Me)$_3^T$**, **Cu_{29}-P(Ph-Cl)$_3^T$**, and **Cu_{28}-PPh_2Py^T**) following geometry optimization using the GGA: PBE/DND method and the Dmol^3 package[60–62] confirmed that these structures are stable (Fig. S19†). The geometric details of the Cu@Cu_{12} kernels of **Cu_{29}-P(Ph-Me)$_3^T$**, **Cu_{29}-P(Ph-Cl)$_3^T$**, and **Cu_{28}-PPh_2Py^T** are listed in Table S4.† The positions of the hydrogens in these three nanoclusters are more intuitively compared in Fig. S15–S18.† All four μ_3-H-Cu_3 (μ_3-H-1/2/3/4-Cu_3) units are located in the $Cu_6(SR)_6$ ring in Cu_{25}, and three μ_4-H-Cu_4 (μ_3-H-5/6/7-Cu_4) moieties are capped by three $Cu_2(SR)_5$ motifs, and three μ_4-H-Cu_4 (μ_3-H-8/9/10-Cu_4) units are capped by three $Cu_3(SR)_6$ units (Fig. S15†). The four μ-H-Cu_3 (μ-H-1/2/3/4-Cu_3) units in **Cu_{29}-P(Ph-Me)$_3$** and **Cu_{28}-PPh_2Py** are also located in their $Cu_6(SR)_6$ rings, while three μ-H-Cu_3 (μ-H-1/2/3/-Cu_3) moieties are located in the $Cu_6(SR)_6$ ring of **Cu_{29}-P(Ph-Cl)$_3$**, and one μ-H-Cu_3 moiety is located in the $Cu_6(SR)_3Cl_3$ ring.

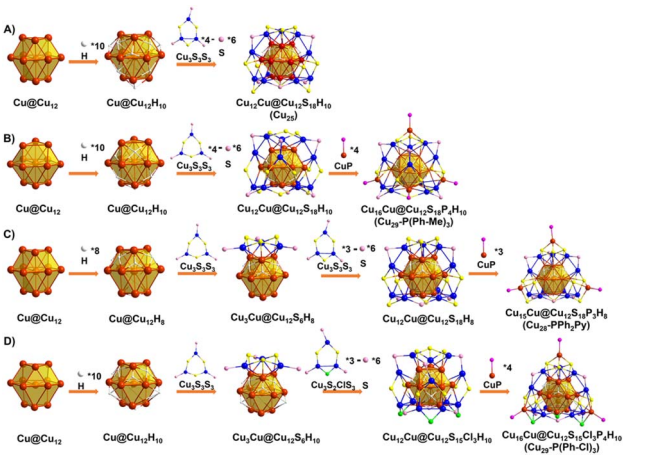

Fig. 5 Structural anatomies of the three nanoclusters: (A) Cu_{25}, (B) Cu_{29}-P(Ph-Me)$_3^T$, (C) Cu_{28}-PPh_2Py^T, and (D) Cu_{29}-P(Ph-Cl)$_3^T$. All carbon, hydrogen, and nitrogen atoms are omitted for clarity. Color scheme: copper = Cu, blue = Cu, yellow = S, pink = S, purple = P, white = H, and green = Cl.

Furthermore, six μ-H-Cu_4 (μ-H-5/6/7/8/9/10-Cu_4) moieties are capped by six $Cu_2(SR)_5$ motifs in **Cu_{29}-P(Ph-Me)$_3$** (Fig. S16†), three μ-H-Cu_4 (μ-H-5/6/7-Cu_4) units are capped by three $Cu_2(SR)_5$ motifs, and three μ-H-Cu_4 (μ-H-8/9/10-Cu_4) moieties are capped by three $Cu_3(SR)_5Cl$ units in the case of **Cu_{29}-P(Ph-Cl)$_3$** (Fig. S17†), while three μ-H-Cu_4 (μ-H-5/6/7-Cu_4) units are capped by three $Cu_2(SR)_5$ motifs, and only one μ-H-Cu_4 (μ-H-8-Cu_4) is capped by $Cu_3(SR)_6$ in the case of **Cu_{28}-PPh$_2$Py** (Fig. S18†). These observations provide a reference for predicting the number and locations of the hydrogen atoms in the nanocluster framework.

Furthermore, the HNMR spectra of these three copper-hydride nanoclusters were carefully obtained *via* dissolving crystals in the solvent (Fig. S26–S28†). For the ^{2}HNMR of **Cu_{28}-PPh$_2$Py-D** (Fig. S26B†), four different D atom signal peaks can be observed, with intensity ratios of about 3 : 1 : 1 : 3. Broadened signal peaks can be observed for the D signal in the ^{2}HNMR spectra of **Cu_{29}-P(Ph-Me)$_3$-D**. And there also were about 4D in the upfield region (low ppm), and about 6D in the low-field region (high ppm) (Fig. S27B†). The deuterium signal ratio at upfield and low-field was 6 : 4.13 for **Cu_{29}-P(Ph-Cl)$_3$-D** (Fig. S28B†). Combining the optimized geometry, ^{2}HNMR data, and the peak position of the D in $Cu_{25}H_{10}$:[59] (i) for **Cu_{28}-PPh$_2$Py-D**, the 4D ($3D_a$ + $1D_b$) in the upfield region (low ppm) can be attributed the H-1, H-2, H-3, and H-4 and the 4D ($1D_c$ + $3D_d$) in the low-field region (high ppm) can be attributed to H-5, H-6, H-7, and H-8 (Fig. S17† and the inset of Fig. S26B†); (ii) for **Cu_{29}-P(Ph-Me)$_3$-D**, the 4D ($4D_a$) in the upfield region (low ppm) can be attributed the H-1, H-2, H-3, and H-4 and the 6D ($6D_d$) observed in the low-field region (high ppm) can be attributed to H-5, H-6, H-7, H-8, H-9 and H10 (Fig. S16† and the inset of Fig. S27B†). In contrast to four different D atoms (D_a, D_b, D_c, and $D_{d)}$ of **Cu_{28}-PPh$_2$Py-D**, **Cu_{29}-P(Ph-Me)$_3$-D** has two D atoms, *viz.*, D_a and D_d, due to the high symmetry; (iii) for **Cu_{29}-P(Ph-Cl)$_3$-D**, the 4D ($3D_a$ + $1D_b$) in the upfield region (low ppm) can be attributed the H-1, H-2, H-3, and H-4 and the 6D ($3D_c$ + $3D_d$) in the low-field region (high ppm) can be attributed to H-5, H-6, H-7, H-8, H-9 and H-10 (Fig. S18† and the inset of Fig. S28B†). From the information of ^{2}HNMR spectra, the signal peak of hydrogen of can be better attributed. The 46H located between 7 ppm and 9 ppm were assigned to hydrogen from PPh_2Py (3 × 14) and 4 $H_{c/d}$ in the cluster. Due to the influence of N on PPh_2Py, part of the hydrogen is significantly shifted, *i.e.* the hydride resonance (3H) at 8.76 ppm. The signal in the alkane region (206H) was due to the thiol and H-ligands (Cal. 18 × 11 + 4(H_a/H_b) = 204H, and Δ = 2H) (Fig. S26†). In the ^{1}HNMR spectrum of **Cu_{29}-P(Ph-Me)$_3$-H**, 52H in the aromatic region belonged to the $-C_6H_4R$ of P(Ph-Me)$_3$ (4 × 4 × 3) and 6 H_d in the cluster, and the 237.63H were attributed to the thiol, H-ligands and $-CH_3$ in P(Ph-Me)$_3$ (Cal. 18 × 11 + 4(H_a) + 4 × 3 × 3 = 238H) (Fig. S27A†). Similarly, 52H in the aromatic region belonged to the $-C_6H_4-$ of P(Ph-Cl)$_3$ and 6 $H_{c/d}$ in the cluster, and the 228.12H were attributed to the thiol, H-ligands (Cal. 15 × 15 + 4($H_{a/b}$) = 229H) (Fig. S28A†).Based on the this information, we can reasonably consider that the hydrogen located in the upfield was the hydrogen (on the cluster surface) covering the Cu_3 surface of the Cu_{13} core, and the hydrogens encapsulated in trigonal prismatic (tp) cages were located in the low-field region, which in turn showed the rationality of predicting the hydrogen positions in the three clusters.

Surface-defect growth and enhanced overall symmetry affect the stability of copper-hydride nanoclusters. The thermal stabilities of these copper-hydride nanoclusters were explored by storing CH_2Cl_2 solutions of **Cu_{29}-P(Ph-Me)$_3$**, **Cu_{29}-P(Ph-Cl)$_3$**, and **Cu_{28}-PPh$_2$Py** at room temperature for a week (Fig. S29†). Fig. S29A† reveals that **Cu_{28}-PPh$_2$Py** starts to decompose after three days, accompanied by precipitation, while some flocs began to form on the fifth day in the **Cu_{29}-P(Ph-Cl)$_3$** solution (Fig. S29B†). In contrast, the solution of **Cu_{29}-P(Ph-Me)$_3$** remained stable for 5 days (Fig. S29C†). Furthermore, a solution of **Cu_{29}-P(Ph-Me)$_3$** in $CHCl_3$ was stable for more than 5 h in an oil bath at 50 °C, while these conditions destroyed both **Cu_{29}-P(Ph-Cl)$_3$** and **Cu_{28}-PPh$_2$Py** (Fig. S30†). In this context, **Cu_{29}-P(Ph-Me)$_3$** is the most stable, followed by **Cu_{29}-P(Ph-Cl)$_3$** and **Cu_{28}-PPh$_2$Py**. The metastability exhibited by **Cu_{28}-PPh$_2$Py** is ascribable to surface vacancy defects that result in incomplete capping of the nanocluster surface. In comparison, **Cu_{29}-P(Ph-Me)$_3$**, which has a standard tetrahedral structure, is more stable than **Cu_{29}-P(Ph-Cl)$_3$**.

4. Conclusions

We synthesized and identified three copper hydride nanoclusters through ligand engineering, including $[Cu_{28}(S\text{-}c\text{-}C_6H_{11})_{18}(PPh_2Py)_3H_8](BF_4)$, a surface-vacancy-defective nanocluster, and $[Cu_{29}(SAdm)_{15}Cl_3(P(Ph\text{-}Cl)_3)_4H_{10}](PF_6)$ and $[Cu_{29}(S\text{-}c\text{-}C_6H_{11})_{18}(P(Ph\text{-}^pMe)_3)_4H_{10}](BF_4)$, which are both non-defective nanoclusters. Because there are few reports on the series of the defect- and defect-growth-based copper-hydride clusters, the series of well-characterized copper nanoclusters prepared in this study provides insight into surface-vacancy-defect to non-defect structural evolution. Structural adjustments were observed in the metal core, hydrogen ligand, metal shell, core/shell bonding pattern, and packing mode during the evolution of surface-vacancy-defective **Cu_{28}-PPh$_2$Py** to non-defective **Cu_{29}-P(Ph-Cl)$_3$** and then to the other **Cu_{29}-P(Ph-Me)$_3$**. Specifically: (i) the anti-cuboctahedral Cu_{13} core is maintained between **Cu_{28}-PPh$_2$Py** and **Cu_{29}-P(Ph-Cl)$_3$**, but changes to a cuboctahedral Cu_{13} structure in **Cu_{29}-P(Ph-Me)$_3$**. (ii) The doubly charged **Cu_{28}-PPh$_2$Py** is embedded with eight hydrides, while singly charged **Cu_{29}-P(Ph-Cl)$_3$/Cu_{29}-P(Ph-Me)$_3$** is embedded with 10 hydrides; however, the positions of the hydrogens are very similar in both clusters. (iii) The $Cu_{16}(SR)_{18}P_4$ shell in **Cu_{29}-P(Ph-Me)$_3$** contains four identical $Cu_4S_6P_1$ motifs assembled by sharing six SR ligands, in which four $Cu_4S_6P_1$ motifs cover the four triangular surfaces (Cu_3) of the cuboctahedral Cu_{13}. On the other hand, the $Cu_{16}(SR)_{18}P_4$ shell in **Cu_{29}-P(Ph-Cl)$_3$** is an assembly of one $Cu_4(SR)_6P_1$ motif that covers the triangular surfaces (Cu_3) and three $Cu_4(SR)_5ClP_1$ motifs that cover the quadrilateral surface (Cu_4) of the anti-cuboctahedral Cu_{13}. As was observed for **Cu_{29}-P(Ph-Cl)$_3$**, **Cu_{28}-PPh$_2$Py** is assembled from one $Cu_4(SR)_6P_1$ motif that covers the triangular surfaces (Cu_3), two $Cu_4(SR)_6P_1$ motifs that cover the quadrilateral surface (Cu_4), and one defective $Cu_3(SR)_6$ unit that covers the quadrilateral surface (Cu_4), which leads to a complex bonding

environment. (iv) Cu_{29}-P(Ph-Me)$_3$ shows a 6H pattern in the crystal lattice, whereas Cu_{28}-PPh_2Py and Cu_{29}-P(Ph-Cl)$_3$ only show 2H arrangements. (v) Stability improved in moving from Cu_{28}-PPh_2Py to Cu_{29}-P(Ph-Cl)$_3$ and then to Cu_{29}-P(Ph-Me)$_3$, which indicates that surface defects, as well as the symmetry of the overall structure, affect the stability of the copper-hydride cluster. The structural evolution observed in moving from surface-vacancy-defective Cu_{28}-PPh_2Py to non-defective Cu_{29}-P(Ph-Cl)$_3$ and then to the other non-defective Cu_{29}-P(Ph-Me)$_3$ enables the structural evolution and the mechanism responsible for the physicochemical properties to be understood and provides valuable insight into the structural surface vacancies in copper nanoclusters and their structure–property relationships.

Data availability

All the data supporting this article have been included in the main text and the ESI.†

Author contributions

Y. B. and B. Y. carried out the experiments, analyzed the data, and wrote the manuscript. X. K. revised the manuscript. X. W. and H. Y. completed DFT calculations. Z. L. and H. D. assisted in the synthesis of nanoclusters. M. Z., S. C., and S. J. designed the project, analyzed the data, and revised the manuscript.

Conflicts of interest

The authors declare no competing financial interests.

Acknowledgements

We acknowledge the financial support provided by the National Natural Science Foundation of China (21901001, 21871001, and 21631001), Ministry of Education and Education Department of Anhui Province, andAnhui Provincial Natural Science Foundation (No. 1908085QB54), and acknowledge the technical support of the high-performance computing platform of Anhui University.

Notes and references

1 R. Jin, C. Zeng, M. Zhou and Y. Chen, *Chem. Rev.*, 2016, **116**, 10346–10413.
2 I. Chakraborty and T. Pradeep, *Chem. Rev.*, 2017, **117**, 8208–8271.
3 R. Jin, G. Li, S. Sharma, Y. Li and X. Du, *Chem. Rev.*, 2021, **121**, 567–648.
4 S. Y. Qian, Z. P. Wang, Z. X. Zuo, X. M. Wang, Q. Wan and X. Yuan, *Coord. Chem. Rev.*, 2022, **451**, 214268.
5 Y. Xiao, Z. Wu, Q. Yao and J. Xie, *Aggregate*, 2021, **2**, 114–132.
6 X. Wei, H. L. Shen, C. Xu, H. Li, S. Jin, X. Kang and M. Z. Zhu, *Inorg. Chem.*, 2021, **60**, 5931–5936.
7 M. R. Friedfeld, J. L. Stein, A. Ritchhart and B. M. Cossairt, *Acc. Chem. Res.*, 2018, **51**, 2803–2810.
8 R. S. Dhayal, W. E. Van Zyl and C. W. Liu, *Acc. Chem. Res.*, 2016, **49**, 86–95.
9 Q. Z. Li, B. Y. Huang, S. Yang, H. Zhang, J. S. Chai, Y. Pei and M. Z. Zhu, *J. Am. Chem. Soc.*, 2021, **143**, 15224–15232.
10 Z. Gan, J. Chen, L. Liao, H. Zhang and Z. K. Wu, *J. Phys. Chem. Lett.*, 2018, **9**, 204–208.
11 D. Crasto, S. Malola, G. Brosofsky, A. Dass and H. Häkkinen, *J. Am. Chem. Soc.*, 2014, **136**, 5000–5005.
12 W. J. Du, S. Deng, S. Chen, S. Jin, Y. Zhen, Y. Pei and M. Z. Zhu, *J. Phys. Chem. Lett.*, 2021, **12**, 6654–6660.
13 G. Li, Z. Lei and Q.-M. Wang, *J. Am. Chem. Soc.*, 2010, **132**, 17678–17679.
14 S. Jin, S. X. Wang, Y. B. Song, M. Zhou, J. Zhong, J. Zhang, A. D. Xia, Y. Pei, M. Chen, P. Li and M. Z. Zhu, *J. Am. Chem. Soc.*, 2014, **136**, 15559–15565.
15 S. Jin, S. X. Wang, L. Xiong, M. Zhou, S. Chen, W. J. Du, A. D Xia, Y. Pei and M. Z. Zhu, *Chem. Mater.*, 2016, **28**, 7905–7911.
16 Y. Zhou, L. W. Liao, S. L. Zhuang, Y. Zhao, Z. B. Gan, W. M. Gu, J. Li, H. T. Deng, N. Xia and Z. K. Wu, *Angew. Chem., Int. Ed.*, 2021, **60**, 8668–8672.
17 J.-S. Yang, Z. Han, X.-Y. Dong, P. Luo, H.-L. Mo and S.-Q. Zang, *Angew. Chem., Int. Ed.*, 2020, **59**, 11898–11902.
18 Y. Negishi, T. Nakazak, S. Malol, S. Takano, Y. Niihor, W. Kurashige, S. Yamazoe, T. Tsukuda and H. Häkkine, *J. Am. Chem. Soc.*, 2015, **137**, 1206–1212.
19 Y. W. Li and R. Jin, *J. Am. Chem. Soc.*, 2020, **142**, 13627–13644.
20 X. Kang, Y. Li, M. Zhu and R. Jin, *Chem. Soc. Rev.*, 2020, **49**, 6443–6514.
21 Y. W. Li, M. Zhou, Y. B. Song, T. Higaki, H. Wang and R. C. Jin, *Nature*, 2021, **594**, 380–384.
22 Q. F. Yao, Z. N. Wu, Z. H. Liu, Y. Z. Lin, X. Yuan and J. P. Xie, *Chem. Sci.*, 2021, **12**, 99–127.
23 Y.-M. Su, Z. Wang, C.-H. Tung, D. Sun and S. K. Schein, *J. Am. Chem. Soc.*, 2021, **143**, 13235–13244.
24 K. Nakamae, M. Tanaka, B. Kure, T. Nakajima, Y. Ura and T. Tanase, *Chem.–Eur. J.*, 2017, **23**, 9457–9461.
25 K. Nakamae, T. Nakajima, Y. Ura, Y. Kitagawa and T. Tanase, *Angew. Chem., Int. Ed.*, 2020, **59**, 2262–2267.
26 (*a*) R. S. Dhayal, J.-H. Liao, Y.-R. Lin, P.-K. Liao, S. Kahlal, J.-Y. Saillard and C. W. Liu, *J. Am. Chem. Soc.*, 2013, **135**, 4704–4707; (*b*) J.-H. Liao, R. S. Dhayal, X. P. Wang, S. Kahlal, J.-Y. Saillard and C. W. Liu, *Inorg. Chem.*, 2014, **53**, 11140–11145.
27 R. S. Dhayal, J.-H. Liao, X. Wang, Y.-C. Liu, M.-H. Chiang, S. Kahlal, J.-Y. Saillard and C. W. Liu, *Angew. Chem., Int. Ed.*, 2015, **54**, 13604–13608.
28 R.-W. Huang, J. Yin, C. Dong, P. Maity, M. Nejib Hedhili, S. Nematulloev, B. Alamer, A. Ghosh, O. F. Mohammed and O. M. Bakr, *ACS Mater. Lett.*, 2021, **3**, 90–99.
29 T. A. Nguyen, Z. R. Jones, B. R. Goldsmith, W. R. Buratto, G. Wu, S. L. Scott and T. W. A. Hayton, *J. Am. Chem. Soc.*, 2015, **137**, 13319–13324.
30 A. L. Chen, X. Kang, S. Jin, W. J. Du, S. X. Wang and M. Z. Zhu, *J. Phys. Chem. Lett.*, 2019, **10**, 6124–6128.
31 A. J. Edwards, R. S. Dhayal, P.-K. Liao, J.-H. Liao, M.-H. Chiang, R. O. Piltz, S. Kahlal, J.-Y. Saillard and C. W. Liu, *Angew. Chem., Int. Ed.*, 2014, **53**, 7214–7218.

32 X. H. Liu, H. Shen, Y. Gao, G. C. Deng, H. W. Deng, Y.-Z. Han, B. K. Teo and N. F. Zheng, *Chem. Commun.*, 2022, **58**, 7670–7673.
33 Q. L. Guo, B.-L. Han, C.-F. Sun, Z. Wang, Y. W. Tao, J.-Q. Lin, G.-G. Luo, C.-H. Tung and D. Sun, *Nanoscale*, 2021, **13**, 19642–19649.
34 R. Kumar Barik, S.-C. Huo, C.-Y. Wu, T.-H. Chiu, J.-H. Liao, X. P. Wang, S. Kahlal, J.-Y. Saillard and C. W. Liu, *Chem.–Eur. J.*, 2020, **26**, 10471–10479.
35 R. S. Dhayal, J.-H. Liao, S. Kahlal, X. Wang, Y.-C. Liu, M.-H. Chiang, W. E. van Zyl, J.-Y. Saillard and C. W. Liu, *Chem.–Eur. J.*, 2015, **21**, 8369–8374.
36 R. S. Dhayal, H.-P. Chen, J.-H. Liao, W. E. van Zyl and C. W. Liu, *ChemistrySelect*, 2018, **3**, 3603–3610.
37 P. Yuan, R. Chen, X. Zhang, F. Chen, J. Yan, C. Sun, D. Ou, J. Peng, S. Lin, Z. Tang, B. K. Teo, L. S. Zheng and N. F. Zheng, *Angew. Chem., Int. Ed.*, 2019, **58**, 835–839.
38 A. Ghosh, R.-W. Huang, B. Alamer, E. Abou-Hamad, M. Nejib Hedhili, O. F. Mohammed and O. M. Bakr, *ACS Mater. Lett.*, 2019, **1**, 297–302.
39 R. W. Huang, J. Yin, C. Dong, A. Ghosh, M. J. Alhilaly, X. Dong, M. Hedhili, E. Abou-Hamad, B. Alamer, S. Nematulloev, Y. Han, O. Mohammed and O. M. Bakr, *J. Am. Chem. Soc.*, 2020, **142**, 8696–8705.
40 A. Baghdasaryana and T. Bürgi, *Nanoscale*, 2021, **13**, 6283–6340.
41 A. Sagadevan, A. Ghosh, P. Maity, O. F. Mohammed, O. M. Bakr and M. Rueping, *J. Am. Chem. Soc.*, 2022, **144**, 12052–12061.
42 Q. Tang, Y. J. Lee, D.-Y. Li, W. Choi, C. W. Liu, D. Lee and D.-E. Jiang, *J. Am. Chem. Soc.*, 2017, **139**, 9728–9736.
43 C.-Y. Liu, S.-F. Yuan, S. Wang, Z.-J. Guan, D.-E. Jiang and Q.-M. Wang, *Nat. Commun.*, 2022, **13**, 2082.
44 P.-K. Liao, C.-S. Fang, A. Edwards, S. Kahlal, J.-Y. Saillard and C. W. Liu, *Inorg. Chem.*, 2012, **51**, 6577–6591.
45 S. Lee, M. S. Bootharaju, G. Deng, S. Malola, W. Baek, H. Häkkinen, N. F. Zheng and T. Hyeon, *J. Am. Chem. Soc.*, 2020, **142**, 13974–13981.
46 S. Lee, M. S. Bootharaju, G. Deng, S. Malola, H. Häkkine, N. F. Zheng and T. Hyeon, *J. Am. Chem. Soc.*, 2021, **143**, 12100–12107.
47 C. W. Dong, R. Wu Huang, C. L. Chen, J. Chen, S. Nematulloev, X. R. Guo, A. Ghosh, B. Alamer, M. N. Hedhili, T. T. Isimjan, Y. Han, O. F. Mohammed and O. M. Bakr, *J. Am. Chem. Soc.*, 2021, **143**, 11026–11035.
48 R. P. B. Silalahi, Q. Wang, J.-H. Liao, T.-H. Chiu, Y.-Y. Wu, X. P. Wang, S. Kahlal, J.-Y. Saillard and C. W. Liu, *Angew. Chem., Int. Ed.*, 2022, **61**, e202113266.
49 K. K. Chakrahari, J. P. Liao, R. P. Brocha Silalahi, T.-H. Chiu, J.-H. Liao, X. P. Wang, S. Kahlal, J.-Y. Saillard and C. W. Liu, *Small*, 2021, **17**, 2002544.
50 X. Kang, M. Zhou, S. X. Wang, G. D. Sun, M. Z. Zhu and R. C. Jin, *Chem. Sci.*, 2017, **8**, 2581–2587.
51 F. Hu, J.-J. Li, Z.-J. Guan, S.-F. Yuan and Q.-M. Wang, *Angew. Chem., Int. Ed.*, 2020, **59**, 5312–5315.
52 X. J. Zou, Y. Lv, X. Kang, H. Z. Yu, S. Jin and M. Z. Zhu, *Inorg. Chem.*, 2021, **60**, 14803–14809.
53 S. F. Yuan, P. Li, Q. Tang, X.-K. Wan, Z.-A. Nan, D.-E. Jiang and Q.-M. Wang, *Nanoscale*, 2017, **9**, 11405–11409.
54 K. K. Chakrahari, J.-H. Liao, S. Kahlal, Y.-C. Liu, M.-H. Chiang, J.-Y. Saillard and C. W. Liu, *Angew. Chem., Int. Ed.*, 2016, **55**, 14704–14708.
55 K. K. Chakrahari, R. P. Brocha Silalahi, J.-H. Liao, S. Kahlal, Y.-C. Liu, J.-F. Lee, M.-H. Chiang, J.-Y. Saillard and C. W. Liu, *Chem. Sci.*, 2018, **9**, 6785–6795.
56 Z. B. Gan, J. S. Chen, J. Wang, C. M. Wang, M.-B. Li, C. H. Yao, S. L. Zhuang, A. Xu, L. L. Li and Z. K. Wu, *Nat. Commun.*, 2017, **8**, 14739.
57 P. Liu and E. J. Hensen, *J. Am. Chem. Soc.*, 2013, **135**, 14032–14035.
58 S. Wang, Z. Wu, S. Dai and D.-E. Jiang, *Angew. Chem., Int. Ed.*, 2021, **60**, 12289–12292.
59 C. Sun, N. Mammen, S. Kaappa, P. Yuan, G. Deng, C. Zhao, J. Yan, S. Malola, K. Honkala, H. Häkkinen, B. K. Teo and N. F. Zheng, *ACS Nano*, 2019, **13**, 5975–5986.
60 J. Perdew, K. Burke and M. Ernzerhof, *Phys. Rev. Lett.*, 1996, **77**, 3865–3868.
61 B. Delley, *J. Chem. Phys.*, 1990, **92**, 508–517.
62 B. Delley, *J. Chem. Phys.*, 2000, **113**, 7756–7764.